Manipulation of High-Fidelity Sidebands under Large Detuning by Floquet Technology: Application to Multi-Mode Cooling

Xue-Ying Yang(杨雪滢)[1], Zi-Dong Lin(林子栋)[2], Shu-Ying Mu(穆姝颖)[1], Wei Wu(吴伟)[1], Chun-Wang Wu(吴春旺)[1], Yi Xie(谢艺)[1], and Ping-Xing Chen(陈平形)[1*]

[1]*Institute for Quantum Science and Technology, College of Sciences, National University of Defense Technology, Changsha 410073, China*

[2]*Shenzhen Institute for Quantum Science and Engineering and Department of Physics, Southern University of Science and Technology, Shenzhen 518055, China*

(Received 19 September 2024; accepted manuscript online 10 October 2024)

The Floquet technology, a powerful way to manipulate quantum states, is employed to drive sidebands transition under large detuning. Our results demonstrate that high fidelities over 99% can be achieved through optimizing suitable modulation frequencies under large detuning. We observe high-fidelity transitions within a high bandwidth by utilizing a single modulation frequency and reveal that this capability is due to the emergence of a flat-band structure in the bandwidth range. The key finding of high-fidelity sideband manipulation under large detuning is experimentally confirmed in nuclear magnetic resonance platform. Finally, we propose a new parallel sideband cooling scheme that enables simultaneous cooling of multiple motional modes. This approach improves the cooling rate compared to conventional schemes with fixed laser frequency and power, and eliminates the need for mode-specific addressing. Our Floquet parallel scheme is applicable to any harmonic oscillator system and is not limited by bandwidth in theory.

DOI: 10.1088/0256-307X/41/11/113702

Cooling harmonic oscillators to approach their motional ground state is crucial in various research fields, including quantum computation and simulation,[1–5] atomic clocks,[6–9] quantum sensing,[10,11] and even gravitational wave detection.[12] Especially for large-scale quantum computing based on ion traps, it is beneficial to cool multiple motional modes simultaneously to near ground states, i.e., high-bandwidth cooling schemes. The standard cooling process for harmonic oscillators often begins with Doppler cooling,[13–16] and then progresses to achieve sub-Doppler cooling such as Sisyphean cooling,[17,18] electromagnetically induced transparency (EIT) cooling,[19–21] and resolution sideband cooling (SBC).[22–24] The SBC technique is often used for sub-Doppler cooling due to its lowest cooling limit, and its effectiveness does not depend on specific atom/ion species or trap geometry.[25,26] Nevertheless, the cooling time increases with the motional modes to be cooled, owing to the limited cooling bandwidth. An enhanced version of the traditional SBC is the parallel SBC, which exhibits a quadratic increase in cooling rate and a substantial expansion in cooling bandwidth.[26] But addressing single ion is a significant challenge for extensive ion chains. Therefore, the demand for high-bandwidth sideband cooling schemes that do not require addressing is particularly pressing, which requires first realizing high-fidelity sideband transitions under large detuning.

Considering the imperative advancements in high bandwidth sideband cooling scheme, Floquet technology emerges as a promising scheme to address the critical limitations. Periodic drive (Floquet modulation) with optimized modulation frequency allows for enhanced simultaneous control of multiple modes and can also be used to enhance the robustness of quantum states against decoherence and dissipation,[27,28] and to improve the fidelity of quantum gates.[29,30] Typically, by applying Floquet modulation to Rydberg atoms, high-fidelity logical gate operations have been achieved, improving the efficiency of quantum qubit interaction.[31] Furthermore, Floquet technology can transform static systems into dynamic ones and drive the system into topological phases without the need for additional modifications.[32–42] More remarkably, compared with the traditional perturbation method, Floquet theory excels in describing strong driving system without being restricted by the rotating wave approximation.[43,44] Floquet modulation has been utilized before in atoms to compensate for Doppler shift, but the modulation frequency depends on the detuning frequency, which is inconvenient for implementation in other experimental platforms.[45] To our best knowledge, no effective high bandwidth sideband cooling scheme based on Floquet modulation has been reported up to date.

In this work, we optimize a suitable modulation frequency to achieve high-fidelity sideband manipulation under large detuning and propose a Floquet modulation scheme to achieve parallel sideband cooling. We first explore the possibility to achieve high-fidelity sideband transitions with a high bandwidth by utilizing a single driving frequency and reveal that this capability is due to the emergence of a flat-band structure in this bandwidth range. Then, the key finding of high-fidelity sideband ma-

*Corresponding author. Email: pxchen@nudt.edu.cn

© 2024 Chinese Physical Society and IOP Publishing Ltd

nipulation under large detuning is confirmed in nuclear magnetic resonance (NMR). Finally, following this insight, we propose a multi-frequency Floquet-driven parallel sideband cooling scheme, in which the laser frequency is fixed while power is modulated. The modulation frequencies are optimized for different phonon modes to cool them simultaneously. Compared to conventional sideband cooling schemes with fixed laser frequency and power, the new parallel scheme offers a significant improvement in cooling rate and does not require addressing. Our Floquet parallel scheme is applicable to any harmonic oscillator system and is not limited by bandwidth in theory.

In this Letter, first we formulate the theoretical model and its related method. Then, the numerical results including experimental validation are presented. The new Floquet-driven parallel sideband cooling scheme is presented. Finally, the main results are summarized.

Theoretical Model. The periodical Hamiltonian $H_{\rm f}(t) = H_{\rm f}(t+T)$ yields a series of equidistant energy bands $\lambda^{\mu} + m\omega_{\rm f} (m \in Z)$ with Floquet eigenenergies λ^{μ} and frequencies $\omega_{\rm f} = 2\pi/T$. Solving the time-dependent Schrödinger equation is now equivalent to the eigenvalue problem of a Floquet matrix:

$$\hat{\mathcal{H}}(t)|\Phi^{\mu}(t)\rangle = [H_{\rm f}(t) - i(\partial/\partial t)]|\Phi^{\mu}(t)\rangle = \lambda^{\mu}|\Phi^{\mu}(t)\rangle, \quad (1)$$

where the Floquet eigenstates $|\Phi^{\mu}(t)\rangle$ have the same period with such a Hamiltonian, and can be decomposed into Fourier series as $|\Phi^{\mu}(t)\rangle = \sum_{m=-\infty}^{+\infty} e^{-im\omega_{\rm f}t}|\Phi_m^{\mu}\rangle$. The state of the system is then a superposition of Floquet eigenstates:

$$|\Psi(t)\rangle = \sum_{\mu} c^{\mu} e^{-it\lambda^{\mu}}|\Phi^{\mu}(t)\rangle = \sum_{\mu,m} c^{\mu}|\Phi_m^{\mu}\rangle e^{-it(m\omega_{\rm f}+\lambda^{\mu})}, \quad (2)$$

with the coefficients c^{μ} determined by the initial conditions at $t = 0$. Combining the Fourier decomposition of $|\Phi^{\mu}(t)\rangle$ and $H_{\rm f}(t) = \sum_m e^{-im\omega_{\rm f}t}H^{(m)}$, which follows from the periodicity of $H_{\rm f}(t)$, Eq. (1) yields

$$(\lambda^{\mu} + m\omega_{\rm f})|\Phi_m^{\mu}\rangle = \sum_{m'} H^{(m-m')}|\Phi_m^{\mu}\rangle. \quad (3)$$

To obtain Floquet eigenvalues and eigenstates, the coefficients in Eq. (3) are rearranged into a time-independent Floquet matrix $\hat{\mathcal{H}}$.

Resolved sideband cooling of a given mode p involves tuning the lasers near resonance with a red sideband (RSB) transition. In this regime, we have an effective Hamiltonian of the form

$$H_{\rm I}^{p} = \eta_p\Omega_{\rm c}(a_p\sigma^{+}e^{-i\delta t} + a_p^{+}\sigma^{-}e^{+i\delta t}). \quad (4)$$

Here, we have considered collective motional models and η_p is the Lamb–Dicke parameter for motional modes p. $\Omega_{\rm c}$ is the Rabi frequency driving the carrier transition $|g\rangle \leftrightarrow |e\rangle$, which is proportional to the square root of the laser power; δ is the detuning of the laser with the RSB; $\sigma^{+}(\sigma^{-}) = |e\rangle\langle g|(|g\rangle\langle e|)$ is the spin-raising (lowering) operator; a_p^{+} (a_p) is the creation (annihilation) operator for phonons in motional modes p. The Hamiltonian is turned on for a duration such that the state evolution under $H_{\rm I}^{p}$ results in a transition from $|g, n_p\rangle$ to $|e, n_p - 1\rangle$, with $|g\rangle$ and $|e\rangle$ being the ground state and excited state of the internal level, and $|n_p\rangle$ the n-th Fock state of the motional state p. This process is repeated until the mode p has been brought to its motional ground state.

Essentially, the effectiveness of sideband cooling is closely related to the fidelity of sideband manipulation. In conventional SBC, the laser frequency and power are fixed, which determines that only the resonant transitions have the highest cooling rate. In what follows, we consider the Floquet modulation of the laser power to drive high fidelity sideband transition under large detuning. We investigate how to eliminate the loss of fidelity induced by frequency detuning by optimizing modulation frequency. We first focus on the case of one motional mode (ignoring subscript p), and its Hamiltonian is given by

$$H_{\rm f}(t) = \Omega_r(t)(a\sigma^{+}e^{-i\delta t} + a^{+}\sigma^{-}e^{+i\delta t}), \quad (5)$$

where $\Omega_r(t) = \eta\Omega_{\rm c}\cos(\omega_{\rm f}t)$ with $\omega_{\rm f}$ being the modulation frequency.

Considering that phonon number n and Floquet energy bands order m are infinite, we diagonalize Hamiltonian (5) in the subspace $\{|e, n\rangle, |g, n+1\rangle\}$ to reduce computational complexity, where $|g\rangle$ and $|e\rangle$ are the ground and excited states of the two-level system, respectively. Then Hamiltonian (5) can be rewritten as

$$H_n(t) = \frac{\delta}{2}\bar{\sigma}_z + \Omega\cos(\omega_{\rm f}t)\sqrt{n+1}\bar{\sigma}_x, \quad (6)$$

where $\Omega = \eta\Omega_{\rm c}$, and the spin-like operators read $\bar{\sigma}_z = |e, n\rangle\langle e, n| - |g, n+1\rangle\langle g, n+1|$, $\bar{\sigma}_x = |g, n+1\rangle\langle e, n| + |e, n\rangle\langle g, n+1|$. Up to now, the Floquet matrix $\hat{\mathcal{H}}$, for a fixed phonon number n, can be expanded into a $2(2m+1) \times 2(2m+1)$ matrix under the basis vectors $|e, n, m\rangle$ and $|g, n+1, m\rangle$. Therefore, we numerically diagonalize the Floquet Hamiltonian $\hat{\mathcal{H}}$ after truncating it to a sufficiently large finite matrix to minimize error.

On the one hand, the periodic Hamiltonian (6) has two nontrivial Floquet eigenenergies λ^{μ}, λ^{ν} and the transitions in the complete Floquet quasienergy bands form Mollow triplets $\omega_{\mu,\nu}^{m} = \Delta m\ \omega_{\rm f} + (\lambda^{\mu} - \lambda^{\nu})$, as shown in Fig. 1(a). If $\mu = \nu$, it corresponds to the center-band transitions (black arrows), and to the side-band transitions (blue or red arrows) otherwise. Based on the Floquet theory [Eq. (2)], Rabi oscillation $P(t)$ exhibits multiple frequency components $\omega_{\mu,\nu}^{m}$. As a result, Rabi oscillation is expected to exhibit consistent behavior with the frequency components $\omega_{\mu,\nu}^{m}$ in the frequency domain.

On the other hand, Hamiltonian (6) satisfies rotational symmetry, and the rotational operator $R = \bar{\sigma}_z$ is time-independent,

$$R\Big[H_n\Big(t + \frac{T}{2}\Big) - i\frac{d}{dt}\Big]R^{-1} = H_n(t) - i\frac{d}{dt}. \quad (7)$$

The Floquet eigenstates have the same symmetry

$$|\Phi^{\mu'}(t)\rangle = \pi_{\mu}^{(R)}R\Big|\Phi^{\mu}\Big(t + \frac{T}{2}\Big)\Big\rangle, \quad (8)$$

with $\pi_{\mu}^{(R)} = e^{i\pi m_{\mu}}$, $m_{\mu} = \{0, 1\}$. This symmetry can be probed through the dynamic dipole matrix elements associated with the probing operator V:[46]

$$V_{\mu,\nu}^{m} = \frac{1}{T}\int_0^T \langle\Phi^{\mu}(t)|V|\Phi^{\nu}(t)\rangle e^{-i\Delta m\ \omega_{\rm f}t}dt, \quad (9)$$

where Δm denotes difference in energy band order. When $R^{\dagger}VR = \alpha_V V$, the dynamical symmetry gives rise to symmetry protected selection rules, such as symmetry-protected dark states (spDSs) for $V^m_{\mu,\nu} = 0$. If choosing $V = \bar{\sigma}_z$, then $R^{\dagger}VR = V$, $\alpha_V = 1$. Combining Eqs. (8) and (9), we obtain

$$V^m_{\nu,\mu} \propto \begin{cases} 1, & \text{if } e^{i\pi(m_\mu - m_\nu + \Delta m)}\alpha_V = 1, \\ 0, & \text{otherwise.} \end{cases} \tag{10}$$

There is no transition when Δm is an odd (even) number for the central bands (sidebands), which is the dark state condition with dynamical rotational symmetry. Figure 1(b) shows the Floquet transition spectrum with solid lines representing the bright states and dashed lines for the dark states.

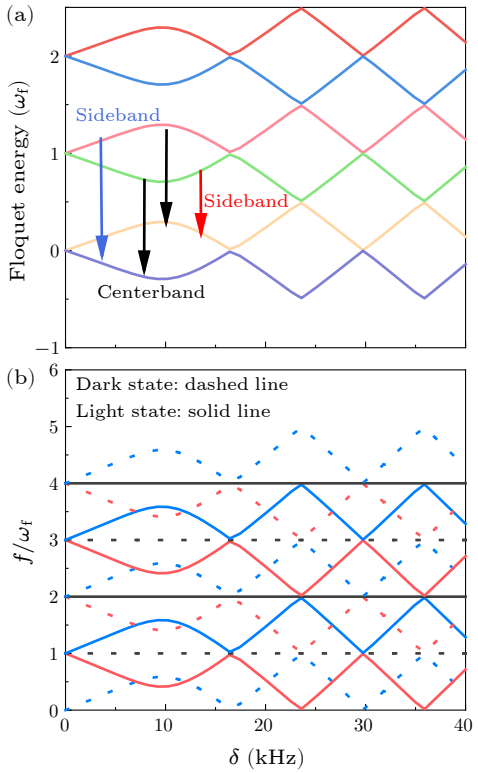

Fig. 1. (a) Floquet quasienergy bands with different detunings. The transition between quasienergies bands have three distinct spectral lines: two degenerate central bands (indicated by black arrows) and two sidebands (indicated by blue and red arrows). (b) Floquet transition spectrum consists of central bands (black lines) and sidebands (blue and red lines) with different detunings. Solid lines represent light states, while dashed lines for dark states. Other parameters are $n = 0$ and $\omega_f = 5.5$ kHz.

To extract the transition elements $V^m_{\mu,\nu}$ between Floquet states, Cappellaro *et al.* developed a protocol that monitors the coherent evolution through projective measurements.[46] This protocol allows us to map the dynamical dipole matrix elements to measure Rabi oscillation amplitudes. Based on such mapping, we are able to effectively extract information about the transitions between Floquet states by the following two steps:

Step 1. From Eq. (2), the expectation value of $\langle V\rangle$ is

$$\langle V\rangle = \langle\Psi(t)|V|\Psi(t)\rangle = \sum_{\mu,\nu,m} c^{\mu *}c^{\nu}e^{i(\lambda^{\mu}-\lambda^{\nu})t}e^{i\Delta m\ \omega_f t}V^m_{\mu,\nu}.$$

The Fourier decomposition of $\langle V\rangle$ reads

$$\langle V\rangle = \sum_{\mu,\nu,m} |A^m_{\mu,\nu}|\cos(\omega^m_{\mu,\nu}t + \phi^m_{\mu,\nu}), \tag{11}$$

with transition frequencies $\omega^m_{\mu,\nu} = \Delta m\ \omega_f + (\lambda^{\mu} - \lambda^{\nu})$. It is found that the Fourier amplitudes $A^m_{\mu,\nu} = 2c^{\mu *}c^{\nu}V^m_{\mu,\nu}$ can be used to extract the dipole matrix elements $V^m_{\mu,\nu}$.

Step 2. For the measurement of Rabi oscillation in this work, the qubit state is projected onto $|g, n+1\rangle$. The $P_{|g,n+1\rangle}(t)$, defined as the probability of being in the $|g, n+1\rangle$ state, presents three classes of frequencies: $\{\Delta m\ \omega_f,\ \Delta m\ \omega_f + (\lambda^{\mu} - \lambda^{\nu}),\ \Delta m\ \omega_f + (\lambda^{\mu} - \lambda^{\nu})\}$. Population $P(t)$ can be transformed into Fourier form

$$P_{|g,n+1\rangle}(t) = \sum_{i,m} |a^m_i|\cos(\omega^m_i t + \phi^m_i), \tag{12}$$

where frequencies ω^m_i and amplitudes $|a^m_i|$ are corresponding to transition frequencies $\omega^m_{\mu,\nu}$ and amplitudes $A^m_{\mu,\nu}$ of Eq. (11), respectively.

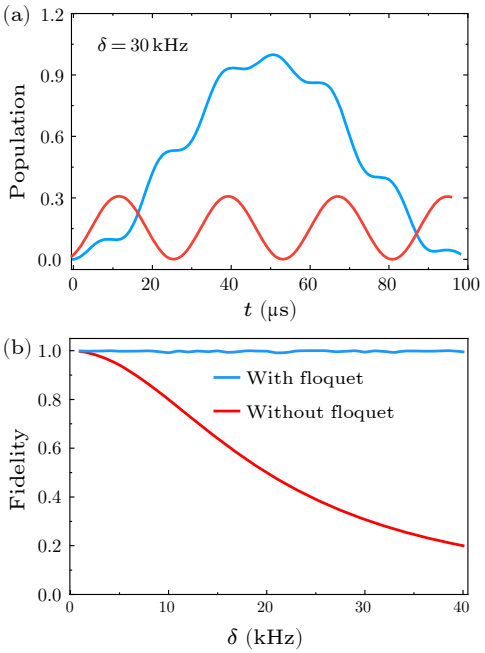

Fig. 2. (a) Normalized ground state $|g, 1\rangle$ population at detuning $\delta = 30$ kHz. The blue lines correspond to the case with Floquet modulation, and its optimized modulation frequency $\omega_f = 29$ kHz. The red lines correspond to the case without Floquet modulation. (b) Numerical results of the fidelity of $|g, 1\rangle$ for different detunings ranging from 0 and 40 kHz. The blue (red) lines correspond to the case with (without) Floquet modulation. The Rabi frequency $\Omega = 20$ kHz.

Simulation Results. Taking a typical transition from initial state $|e, 0\rangle$ to $|g, 1\rangle$ as an example. Figure 2 shows our simulation results. Blue lines represent transition with Floquet modulation, while red lines correspond to no Floquet modulation. Without Floquet modulation, the maximum population of $|g, 1\rangle$ is 0.313 at $\delta = 30$ kHz. In the

presence of Floquet modulation, the results show that the population of $|g, 1\rangle$ is greater than 0.990 for $\omega_{\rm f}$ between 28.5 kHz and 30 kHz, and the highest population of $|g, 1\rangle$ reaches 0.998 at $t = 51\,\mu$s and $\omega_{\rm f} = 29$ kHz. Typical simulation results are shown in Fig. 2(a). The highest population corresponds to the fidelity of the state.

Figure 2(b) shows the fidelity of state $|g, 1\rangle$ for different detunings ranging from 0 to 40 kHz. It is easy to see that the fidelity decreases with detuning for the case without Floquet modulation, while keep unchanged by optimizing the modulation frequency for different detuning δ. Interestingly, our results show that the high fidelity can be achieved by using Floquet modulation even when the detuning δ is twice the Rabi frequency Ω.

The dependence of fidelity on modulation frequency $\omega_{\rm f}$ and detuning δ for different phonon numbers is shown in Fig. 3. For small detunings, the range of applicable modulation frequencies, which can result in high fidelity, forms a continuous region starting from 0. When $n = 0$, $\omega_{\rm f}$ ranging from 0 to 7 kHz can ensure the fidelity greater than 0.99 for $0 < \delta < 2$ kHz. For $n = 3$, the region can attain high fidelities, increasing slightly to $0 < \delta < 3$ kHz and $0 < \omega_{\rm f} < 14$ kHz. When n increases to 8, such region is further expanded to $0 < \delta < 4$ kHz and $0 < \omega_{\rm f} < 20$ kHz. Furthermore, our results show that the suitable region expands with phonon number n. It is interesting to find that for a fixed detuning, the appropriate modulation frequency covers a range of at least 2 kHz, and vice verse. This range becomes far wider for larger phonon number n, which can be used to resist the laser frequency drift and reduce the required accuracy of frequency calibration in real experiments.

One of the main findings of this work can be drawn from Fig. 3, that is, a single optimized modulation frequency can always be found to achieve high fidelity for a quite large detuning range, which increases with phonon number. Typically, for $n = 0$, $\omega_{\rm f} = 5.5$ kHz ensures high fidelity for δ ranging from 0 to 5 kHz, $\omega_{\rm f} = 11$ kHz is selected for δ ranging from 0 to 10 kHz ($n = 3$), and $\omega_{\rm f} = 16$ kHz is for δ ranging from 0 to 18 kHz ($n = 8$).

For small n, the optimized modulation frequency $\omega_{\rm f} \approx \delta$. This can be understood from Hamiltonian (6), where the periodically driven Hamiltonian is similar to the one describing interaction between a single-mode electromagnetic field and a two-level atom. In this case, detuning δ corresponds to the atomic transition frequency, and modulation frequency corresponds to electromagnetic field frequencies. It is worth noting that strong coupling occurs here, $\delta + \omega_{\rm f} \sim \Omega$, and "off resonance ($\delta \neq \omega_{\rm f}$)" can still achieve high fidelity. In our case, increasing the phonons number is equivalent to enhancing the coupling strength, leading to a greater region of high fidelity, as shown in Fig. 3. This provides us another way to realize large stable region experimentally.

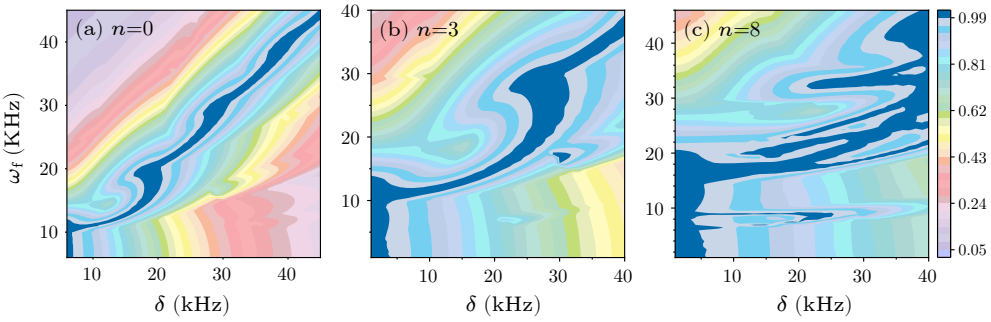

Fig. 3. Dependence of fidelity on modulation frequency $\omega_{\rm f}$ and detuning δ for different phonon numbers: (a) $n = 0$, (b) $n = 3$, and (c) $n = 8$. The dark blue region represents the fidelity exceeding 99%. The Rabi frequency $\Omega = 20$ kHz.

Experimental Validation. We verify sideband transition dynamics under larger detunings on NMR platform. By performing a Trotter–Suzuki decomposition on the time-evolution operator of the key Hamiltonian (6), we convert it into a sequence of rotation gates that are manageable by the platform to achieve quantum simulation.

The experiment is performed on the Gemini Desktop NMR quantum computer.[47,48] Gemini contains two qubits which are the two connected ^{31}P and ^{1}H nuclear spins in Dimethyl phosphite [$(CH_4\ O)_2PH$] molecules. In our experiments, we discretize the time $T_{\rm total}$ into $N_{\Delta t} = 20$ or $N_{\Delta t} = 50$ segments, with each segment having a time step $\Delta t = T_{\rm total}/20$ or $\Delta t = T_{\rm total}/50$. The values of the time step here is consistent with the one used in numerical simulations. The time resolution of the experimental simulation is aligned with that of the numerical computational models, ensuring the validity of the experimental outcomes. In this case, the Hamiltonian of each interval can be approximately regarded to be time-independent. The evolution operator of the i-th segment can be written as

$$U_i = e^{-iH_i t} = e^{-i(\frac{\delta}{2}\sigma_z + \Omega\sqrt{n+1}\cos(\omega_{\rm f}(i-1)\Delta t)\sigma_x)\Delta t}, \quad (13)$$

where H_i corresponds to Eq. (6); δ is detuning and $\omega_{\rm f}$ is modulation frequency. In the limit of a sufficiently small interval Δt, U_i can be easily realized in digital quantum simulation (DQS) using first-order Trotter–Suzuki decomposition:[49]

$$U_i \approx e^{-i\frac{\sigma_z}{2}\theta_i^z} e^{-i\frac{\sigma_x}{2}\theta_i^x} = R_z(\theta_i^z) R_x(\theta_i^x), \quad (14)$$

with $\theta_i^z = \delta\Delta t$, $\theta_i^x = 2\Omega\sqrt{n+1}\cos(\omega_{\rm f}(i-1)\Delta t)\Delta t$. $R_z(\theta_i^z)$ and $R_x(\theta_i^x)$ are the operations that rotate qubit θ_i^z radian around the z-axis and θ_i^x radian around the x-axis, respectively. After applying the Trotter decomposition to the computational model, the approximation is introduced

with the resulting error being around 2%. The precision is sufficient for capturing the effects and phenomena under investigation, affirming the validity of our experimental approach.

The initial state of the two-qubit system is prepared to be a pseudo-pure state.[50] Then $R_z(\theta_i^z)$ and $R_x(\theta_i^x)$ are realized experimentally by built-in arbitrary angle rotation operation in Gemini. At the completion of the circuit, quantum tomography is executed on the phosphorus ^{31}P qubit. Since our experiment aims to portray the progression of quantum states, it is necessary to incrementally scan i from 1 to $N_{\Delta t}$. After that, we can obtain the evolutionary process of the quantum states based on the results yielded from these $N_{\Delta t}$ experiments. For the total evolution time T_{total}, it contains $N_{\Delta t}$ evolution segments, leading to an execution of $2 \times N_{\Delta t}$ gate operations in total.

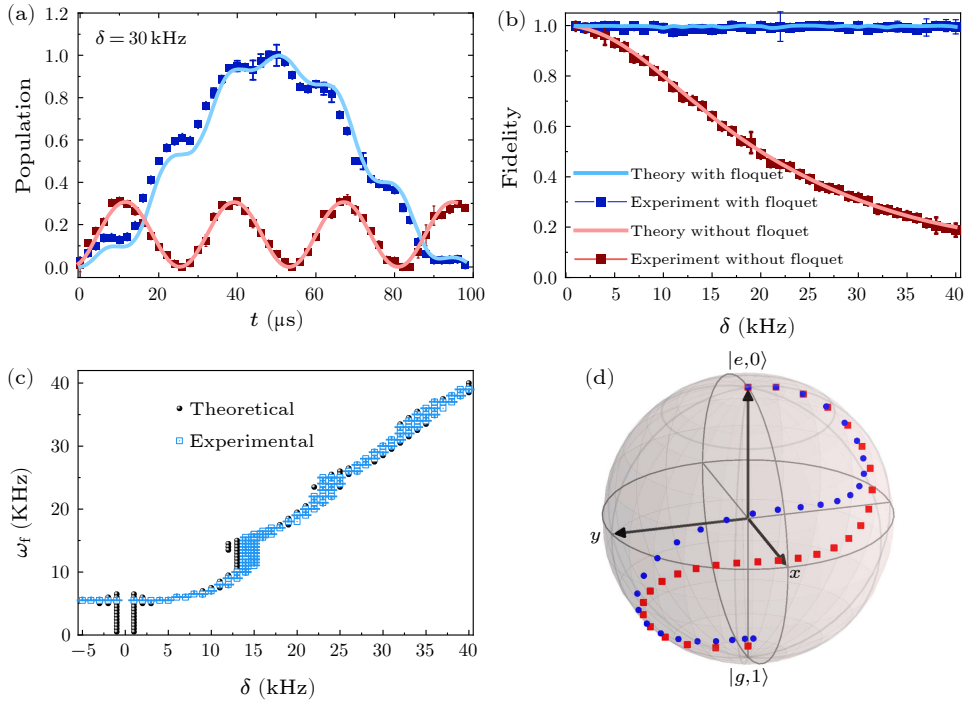

Fig. 4. (a) Normalized ground state $|g, 1\rangle$ population at detuning $\delta = 30$ kHz. The blue lines correspond to the case with Floquet modulation, and its optimized modulation frequency $\omega_f = 29$ kHz. The red lines correspond to the case without Floquet modulation. The solid line represents the numerical results, and the dotted line represents the experimental data. (b) Numerical and experimental results of the fidelity of $|g, 1\rangle$ for different detunings ranging from 0 and 40 kHz. (c) Optimized modulation frequencies ω_f with fidelity exceeding 99% for different detuning δ. (d) The state trajectories on the Bloch sphere for an Floquet π pulse with $\omega_f = 11$ kHz and 16 kHz at $\delta = 15$ kHz. The Rabi frequency $\Omega = 10$ kHz.

We first set the same parameters as in Fig. 2 and verified them in the experimental platform. The results are shown in Figs. 4(a) and 4(b). The solid lines are the theoretical results and the dashed lines are the experimental results. The highest population of $|g, 1\rangle$ reaches 0.998 ± 0.013 at $t = 51$ μs and $\omega_f = 29$ kHz, from which the experimental result agrees well with the simulation result of 0.999. Figure 4(b) shows the fidelity of state $|g, 1\rangle$ for different detunings ranging from 0 to 40 kHz. As predicted by the theory, Floquet modulation retains high fidelity even under large detuning.

Regarding the numerical results presented in Fig. 3, we have performed experimental validations for the parameter regime corresponding to the high-fidelity region at $n = 0$. The outcomes from these experiments are illustrated in Fig. 4(c). The experimental data aligns remarkably well with the theoretical calculations. Consistent with the numerical results observed, multiple modulation frequencies can lead to high fidelity (greater than 0.99) for a fixed detuning. For example, for a detuning $\delta = 15$ kHz, modulation frequencies ranging from 11 to 16 kHz are applicable. Figure 4(d) shows the trajectories of state from $|e, 0\rangle$ to $|g, 1\rangle$ on the Bloch sphere for modulation frequencies of 11 kHz and 16 kHz.

We have also experimentally validated the high fidelity transitions within a high bandwidth by utilizing a single modulation frequency. Table 1 lists the fidelities realized experimentally of special modulation frequency $\omega_f = 5.5$, 11, 16 kHz for different detunings, and for different phonon number $n = 0$, 3, 8. Consistent with the numerical results observed, for $n = 0$, $\omega_f = 5.5$ kHz ensures high fidelity for δ ranging from 0 to 5 kHz, $\omega_f = 11$ kHz is selected for δ ranging from 0 and 10 kHz ($n = 3$), and $\omega_f = 16$ kHz is for δ ranging from 0 and 18 kHz ($n = 8$). However, the fidelity of experimental results does not always match the high level observed in numerical results. The experimental error mainly comes from the noise of the control pulse and the fitting error of the frequency domain signal converted from the free-induction-decay signal during readout. For the selected modulation frequencies, the fidelity decreases with detuning. Consequently, only typical detuning values are presented in Table 1.

Table 1. Fidelities achieved experimentally as a function of modulation frequency and detuning.

		$\delta = 2$ kHz	$\delta = 4$ kHz	$\delta = 5$ kHz	$\delta = 8$ kHz	$\delta = 10$ kHz	$\delta = 12$ kHz	$\delta = 16$ kHz	$\delta = 18$ kHz
$\omega_f = 5.5$ kHz	$n = 0$	0.991±0.015	1.000±0.003	0.990±0.007	0.895±0.021	0.764±0.045	0.698±0.022	0.575±0.022	0.526±0.013
$\omega_f = 11$ kHz	$n = 3$	0.990±0.018	0.989±0.017	0.994±0.045	1.000±0.031	0.983±0.045	0.979±0.022	0.895±0.022	0.791±0.023
$\omega_f = 16$ kHz	$n = 8$	1.000±0.026	1.000±0.036	0.998±0.019	0.986±0.021	0.992±0.045	0.993±0.022	0.981±0.022	0.977±0.031

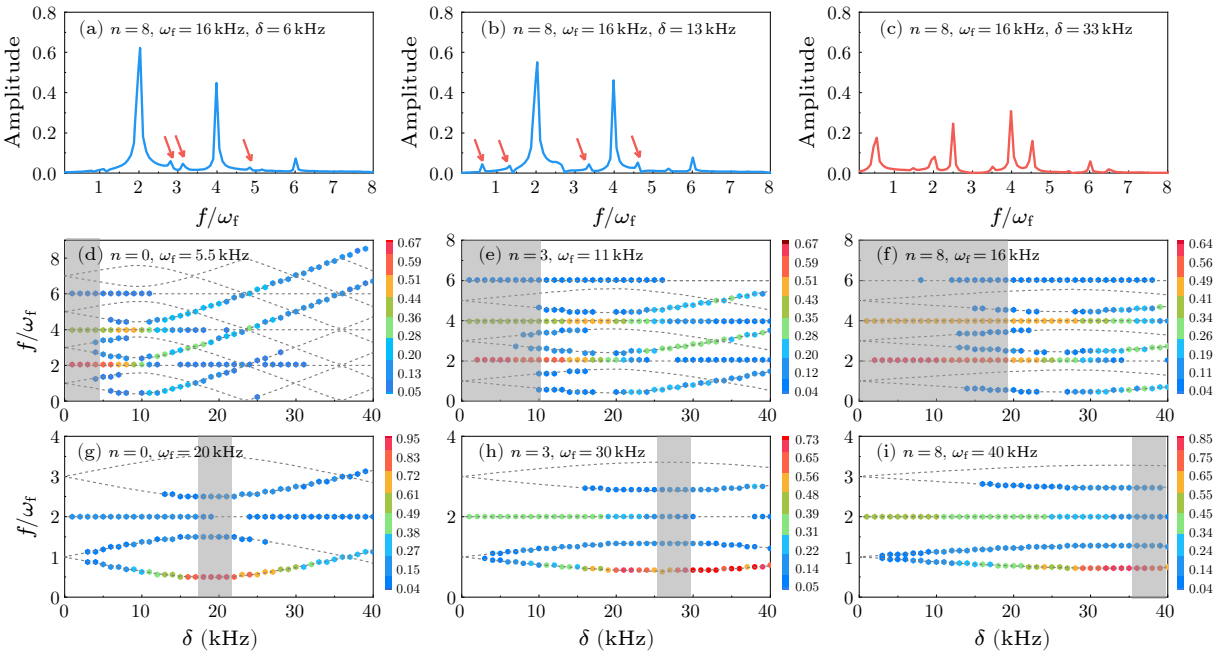

Fig. 5. Rabi oscillations in the frequency domain with fixed $n = 8$ and $\omega_f = 16$ kHz, for different detunings: (a) $\delta = 6$ kHz, (b) $\delta = 13$ kHz, and (c) $\delta = 33$ kHz. The red arrows indicate the ignored frequencies whose amplitudes are less than 0.09 and the amplitude of main frequency exceeds 75% of the total amplitudes. (d)–(i) The Fourier transition spectrum of the Rabi measurements corresponding to the same parameters listed in Table 1. Here the initial state is $|e, 0\rangle$ and we present Rabi oscillations $P_{|g,\, n+1\rangle}$ for different detuning δ, and the detection time is from 0 to 800 μs with 32000 sampling points for fixed detuning. The shaded portions denote the presence of flat bands.

Underlying Physical Picture. To gain more insights of the above results, we study the Floquet transition spectrum at different detunings by calculating Rabi oscillations in the frequency domain. Figures 5(a)–5(c) illustrate the Rabi oscillations in the frequency domain for fixed $n = 8$ and $\omega_f = 16$ kHz, but for varying detuning $\delta = 6$, 13, 33 kHz. As discussed above, if we look at the Rabi oscillation in the frequency domain, the frequencies in Eq. (12) correspond to the transition frequencies in Fig. 1(b), and the amplitudes correspond to the dipole transition matrix element (transition probability). To illustrate the transitions [the light states in Fig. 1(b)] and the transition probability, we transform Figs. 5(a)–5(c) to Fig. 5(f) by using different colors to represent the values of amplitudes. Here we ignore frequencies whose amplitudes are less than 0.09 and the amplitude of main frequency exceeds 75% of the total amplitudes, as indicated by the arrows in Figs. 5(a) and 5(b).

Figures 5(d)–5(i) show the Floquet transition spectrum as functions of detuning for phonon number $n = 0$, 3, 8 and specific modulation frequencies. The modulation frequencies in Figs. 5(d)–5(f) are those listed in Table 1. For such three cases, it is found that the main transitions are the central bands of $\Delta m = 2$ and 4 when the detuning δ is within the range from zero to a frequency slightly larger than the ω_f. When the detuning increases further, the transition probabilities of the central bands decreases quickly, and the transitions of the sidebands occur. For the central band transitions, the frequencies shows no dependence on the detuning δ, while the sideband transition frequencies show strong dependence. Figures 5(g)–5(i) illustrate the main transitions for larger modulation frequencies. For small detuning, the transitions are mainly the central band of $\Delta m = 2$ with small probabilities. Once the detuning δ falls in the range around ω_f, the sideband transition of $\Delta m = 1$ becomes dominated. Thus we can conclude that the high fidelities for large detuning in Fig. 3 can be realized by the sideband transitions, and the transition frequencies keep almost unchanged in such cases (corresponding to the bottom of the red sideband).

The blue regions in Fig. 3 correspond to fidelities greater than 0.99, where flat band structures exists according to the Floquet transition spectra of Fig. 5 (shaded portions). When the main transition is in the central band, the Floquet transition spectrum shows a flat band over a large detuning range, ranging from 0 to 5 kHz, 0 to 10 kHz, and 0 to 16 kHz, as shown in Figs. 5(d), 5(e), and 5(f) for $n = 0$, 3 and 8, respectively. When the main transition is in the sideband, the Floquet transition spectra show a flat band for a narrow detuning range, i.e., 19–21 kHz,

25–30 kHz, and 35–40 kHz for Figs. 5(g), 5(h), and 5(i), respectively. The relatively consistent stability of the main transition frequency against detuning allows for the realization of high fidelity by using even a single modulation frequency. Additionally, all of the transitions in Fig. 5 corresponds to the light states in Fig. 1(b), confirming that the Floquet transition spectra are indeed protected by rotational symmetry.

The above results clearly indicate the ability of the Fourier transition frequency to remain constant within a specific detuning range under a single optimized modulation frequency, which is a significant potential for practical applications. It introduces the possibility of using a single frequency driving, which simplifies the system design and minimizes the complexity while optimizing signal processing and modulation. Recognizing high-fidelity Fourier flat bands under particular parameter combinations also offers valuable insights for system optimization. Beyond aiding in the design and refinement of diverse modulation systems, the practical implications of these findings are profound.

Application: New Floquet Sideband Cooling Scheme. Following this insight, we propose a multi-frequency Floquet-driven parallel sideband cooling scheme. In conventional sideband cooling, the laser power and frequency are fixed, and the cooling process is carried out sequentially for each motional mode p because each mode requires a different resonant frequency. This sequential approach leads to an extended cooling duration. In our new cooling scheme, the laser frequency is fixed while the power is modulated. The matched modulation frequencies are optimized for different phonon modes to cool them simultaneously. The Hamiltonian is given as

$$H_{\rm f}(t) = \frac{1}{p_{\max}} \sum_{p=1}^{p_{\max}} \Omega_{\rm c} \cos(\omega_{\rm f}^{p} t) \times \sum_{p'=1}^{p_{\max}} \eta_{p'} (a_{p'} \sigma^{+} e^{i\delta_{p'} t} + a_{p'}^{\dagger} \sigma^{-} e^{-i\delta_{p'} t}). \quad (15)$$

Here, we have considered $p_{\max}$ collective modes; $\omega_{\rm f}^{p}$ is the modulation frequency for motional mode p, and $\delta_{p'}$ is the detuning between the mode frequencies and the laser frequency. Upon identifying the motional modes that require cooling, the detunings $\delta_{p'}$ are also determined. Substituting Eq. (15) into the master equation yields

$$\dot{\rho} = -i[H_{\rm f}(t), \rho] + \mathcal{L}_{\rm sp}[\rho] + \mathcal{L}_{\rm heat}[\rho], \quad (16)$$

where ρ is the density operator of the system. The spontaneous emission, including the recoil effect, is described by the dissipative Liouvillian term:

$$\mathcal{L}_{\rm sp}[\rho] = \Gamma \Big[\sigma^{-} e^{i \sum_{p=1}^{p_{\max}} \eta_p (a_p + a_p^{\dagger})} \rho e^{-i \sum_{p=1}^{p_{\max}} \eta_p (a_p + a_p^{\dagger})} \sigma^{+} - \frac{1}{2} \{\sigma^{+}\sigma^{-}, \rho\} \Big], \quad (17)$$

where Γ is the spontaneous emission rate, σ^{-} and σ^{+} are the lowering and raising operators of the internal states, and η_p is the Lamb–Dicke parameter for each motional mode. The exponential operators account for the recoil effect on all motional modes. To consider the heating rate due to technical noise, we include an additional dissipative term:

$$\mathcal{L}_{\rm heat}[\rho] = \sum_{p=1}^{p_{\max}} \Gamma_{\rm heat}^{p} \Big(a_p^{\dagger} \rho a_p - \frac{1}{2} \{ a_p a_p^{\dagger}, \rho \} \Big), \quad (18)$$

where $\Gamma_{\rm heat}^{p}$ is the heating rate for motional mode p.

We optimize the modulation frequencies $\omega_{\rm f}^{p}$ for different phonon modes, ensuring that the average phonon number $\bar{n}_p$ for each mode is less than 0.3, approaching the ground state. To confirm the effectiveness of our protocol, we simulate the cooling process in trapped four-ion chain. The trap frequencies are $\{\omega_x, \omega_y, \omega_z, \} = 2\pi \times \{1.706, 1.754, 0.6\}$ MHz to maintain the four-ion crystals in the trap.[51] The frequencies of the eight radial modes are $\{\omega_{pv1}, \omega_{pv2}, \ldots, \omega_{pv8}\} = 2\pi \times \{0, 48.5, 113.2, 168.1, 294.2, 352.4, 552.9, 633.4\}$ kHz $+ \omega_{pv1}$, where $\omega_{pv1} = 1.12$ MHz. The changes in the average phonon number over cooling time with and without Floquet modulation are shown in Fig. 6. The dashed lines represent conventional sideband cooling, while the solid lines correspond to the new Floquet sideband cooling scheme, with different colors indicating different motional modes; the initial phonon number for all is set to 2. It should be stated that the upper limit for the phonon number during both Floquet cooling and traditional sideband cooling is consistent, provided that the sidebands are resolvable within the Lamb–Dicke regime. All the comparisons below are conducted under the condition of equal total laser power for both the schemes.

First, we optimize the first four motional modes, as shown in Fig. 6(a). The optimized modulation frequencies $\omega_{\rm f}$ for these four modes are 89, 40, 29, and 79 kHz, respectively. Within a cooling time of 2000 μs, all four modes under Floquet modulation reach an average phonon number below 0.3. In contrast, traditional sideband cooling can only achieve near-ground-state cooling for the mode that is resonant with the laser. The second mode is close in frequency to the first mode and also nearly cools to the ground state (for numerical simplicity, we only consider the laser resonant with the first mode).

Next, we consider cooling the modes $\{\omega_{pv1}, \omega_{pv4}, \omega_{pv6}, \omega_{pv7}\}$, which have a maximum bandwidth of 5.5 MHz. By optimizing appropriate modulation frequencies $\{\omega_{\rm f}^{p1}, \omega_{\rm f}^{p4}, \omega_{\rm f}^{p6}, \omega_{\rm f}^{p7}\} = 2\pi \times \{284, 116, 67, 268\}$ kHz and setting the laser power to $\Omega_{\rm c} = (2\pi)170$ kHz, these four modes can still be cooled to nearly the ground state within a cooling time of 2000 μs, as shown in Fig. 6(b). In contrast, traditional sideband cooling, due to the large bandwidth, only cools the mode that is resonant with the laser to nearly the ground state.

In Fig. 6(c), we consider cooling the modes $\{\omega_{pv1}, \omega_{pv2}, \omega_{pv7}, \omega_{pv8}\}$. Even with the expanded bandwidth of 6.3 MHz, the Floquet modulation scheme can still effectively cool all four modes to nearly the ground state. To better cover the four modes with traditional sideband cooling, we adjust the laser frequency to the midpoint of the four modes, i.e., $\omega_L = (\omega_{pv1} + \omega_{pv8})/2$. However, the results show that it still cannot cool to the ground state as quickly as the Floquet modulation scheme.

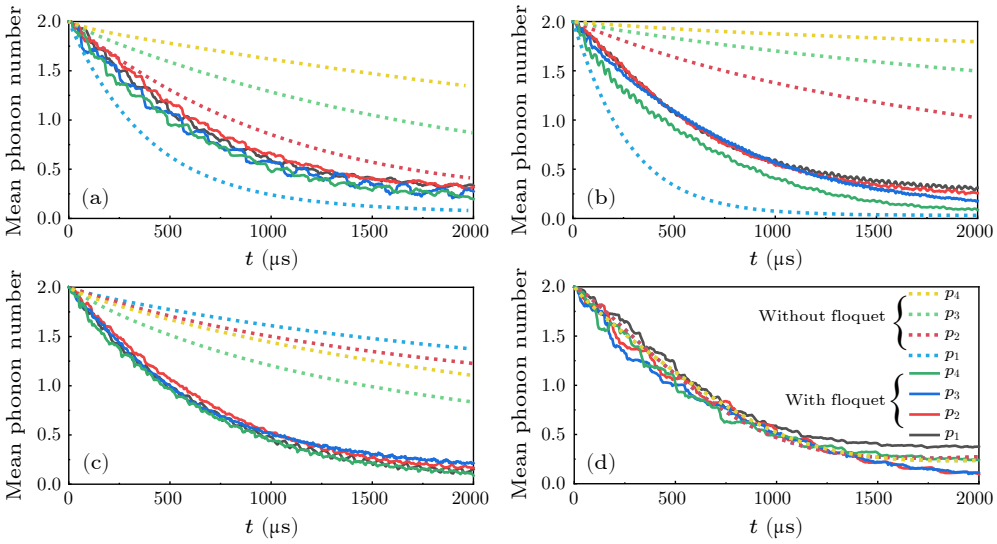

Fig. 6. Average phonon number over cooling time with and without Floquet modulation for different modes p. Dashed lines represent without Floquet modulation, while Solid lines correspond to Floquet modulation. Different colors indicate different modes p; the initial phonon number for all is set to 2. (a) The detuning for the foremost four radial modes $\{\delta_{p1}, \delta_{p2}, \delta_{p3}, \delta_{p4}\} = 2\pi \times \{0, 48.5, 113.2, 168.1\}$ kHz. Corresponding modulation frequency $\{\omega_{\rm f}^{p1}, \omega_{\rm f}^{p2}, \omega_{\rm f}^{p3}, \omega_{\rm f}^{p4}\} = 2\pi \times \{89, 40, 29, 79\}$ kHz. $\Omega_{\rm c} = 100$ kHz. (b) The detuning for four widely spaced modes $\{\delta_{p1}, \delta_{p4}, \delta_{p6}, \delta_{p7}\} = 2\pi \times \{0, 168.1, 352.4, 552.9\}$ kHz. Corresponding modulation frequency $\{\omega_{\rm f}^{p1}, \omega_{\rm f}^{p2}, \omega_{\rm f}^{p3}, \omega_{\rm f}^{p4}\} = 2\pi \times \{284, 116, 67, 268\}$ kHz. $\Omega_{\rm c} = 170$ kHz. (c) The detuning for four widely spaced modes $\{\delta_{p1}, \delta_{p2}, \delta_{p7}, \delta_{p8}\} = 2\pi \times \{0, 48.5, 552.9, 633.4\}$ kHz. Corresponding modulation frequency $\{\omega_{\rm f}^{p1}, \omega_{\rm f}^{p2}, \omega_{\rm f}^{p3}, \omega_{\rm f}^{p4}\} = 2\pi \times \{284, 116, 67, 268\}$ kHz. $\Omega_{\rm c} = 200$ kHz. Laser frequency $\omega_L = (\omega_{pv1} + \omega_{pv8})/2$. (d) Individual addressing traditional sideband cooling scheme versus Floquet modulation cooling scheme applied to the first four phonon modes.

Finally, we adjust the laser in the traditional cooling scheme to be simultaneously resonant with the first four modes, which implies the need for individual addressing in the experiment. The laser power is set to $\Omega_{\rm c} = (2\pi)100$ kHz. The results are shown in Fig. 6(d). The Floquet modulation cooling scheme and the individually addressed sideband cooling demonstrate almost the same cooling rates, with the latter achieving a slightly better cooling limit. In large ion chains, individual addressing becomes practically challenging due to the small spacing between ions and the diffraction limit of light. Crosstalk between ions can lead to unintended excitations, reducing the fidelity of operations. Our Floquet modulation scheme circumvents these challenges by eliminating the need for individual addressing, making it highly suitable for scalable quantum systems.

It is noteworthy that in practical experiments, laser power typically alternates to resonate with these modes for effective cooling. By analyzing Figs. 6(a) and 6(b), we find that when the bandwidth exceeds 2 MHz, the Floquet modulation cooling scheme demonstrates significant advantages. However, when the bandwidth is below this threshold, these advantages are less pronounced.

Compared to conventional sideband cooling schemes, our new Floquet-driven parallel cooling scheme offers the capability to simultaneously cool multiple motional modes with a significant improvement in cooling rate. Additionally, the laser pulse shapes required for this scheme can be easily implemented in experiments using an arbitrary waveform generator, making it highly feasible. Unlike previous methods that require individual addressing to simultaneously cool multiple modes, our approach achieves this without individual addressing. The Hamiltonian involves only global laser illumination, effectively interacting with each motional mode through optimized modulation frequencies. This not only simplifies the experimental setup but also reduces potential crosstalk between ions.

In summary, we have investigated the high-fidelity sideband manipulation under large detuning by Floquet technology and proposed a new scheme to achieve parallel sideband cooling. Our results show that the high fidelity transition can be achieved by using Floquet modulation even when the detuning is large. Specifically, it is shown that a single optimized modulation frequency can always be found to achieve high fidelity for a quite large detuning range. Furthermore, a flat and symmetry-protected Floquet transition spectrum is observed in the Floquet transition spectrum, where different detuning corresponds to the same main transition frequency. In addition, the key finding of high-fidelity sideband manipulation under large detuning is confirmed in NMR, a standardized and universal digital simulation platform, supporting the validity of our results. Building on this insight, we propose a multi-frequency Floquet-driven parallel sideband cooling scheme that optimizes modulation frequencies to simultaneously cool different phonon modes. Our Floquet-driven parallel sideband cooling scheme demonstrates a significant improvement in simultaneously cooling multiple motional modes compared to traditional methods. By optimizing modulation frequencies and appropriately adjusting laser power, we achieve near-ground-state cooling across modes with varying bandwidths. This approach

reduces the cooling duration and mitigates the complexities associated with individual ion addressing in large ion chains.

Acknowledgement. This work is supported by the National Natural Science Foundation of China (Grant Nos. 11904402, 12174447, 12074433, 12004430, and 12174448).

References

[1] Pino J M, Dreiling J M, Figgatt C, Gaebler J P, Moses S A, Allman M S, Baldwin C H, Foss-Feig M, Hayes D, Mayer K, Ryan-Anderson C, and Neyenhuis B 2021 *Nature* **592** 209

[2] Wright K, Beck K M, Debnath S, Amini J M, Nam Y, Grzesiak N, Chen J S, Pisenti N C, Chmielewski M, Collins C, Hudek K M, Mizrahi J, Wong-Campos J D, Allen S, Apisdorf J, Solomon P, Williams M, Ducore A M, Blinov A, Kreikemeier S M, Chaplin V, Keesan M, Monroe C, and Kim J 2019 *Nat. Commun.* **10** 5464

[3] Blatt R and Roos C F 2012 *Nat. Phys.* **8** 277

[4] Monroe C, Campbell W C, Duan L M, Gong Z X, Gorshkov A V, Hess P W, Islam R, Kim K, Linke N M, Pagano G, Richerme P, Senko C, and Yao N Y 2021 *Rev. Mod. Phys.* **93** 025001

[5] Xie H, Yin H, and Fan C 2024 *Chin. Phys. Lett.* **41** 044202

[6] Ludlow A D, Boyd M M, Ye J, Peik E, and Schmidt P O 2015 *Rev. Mod. Phys.* **87** 637

[7] Huntemann N, Sanner C, Lipphardt B, Tamm C, and Peik E 2016 *Phys. Rev. Lett.* **116** 063001

[8] Brewer S M, Chen J S, Hankin A M, Clements E R, Chou C W, Wineland D J, Hume D B, and Leibrandt D R 2019 *Phys. Rev. Lett.* **123** 033201

[9] Lu Y, Zhang R, Song C, Chen C, Si R, and Ning C 2023 *Chin. Phys. Lett.* **40** 093101

[10] Degen C L, Reinhard F, and Cappellaro P 2017 *Rev. Mod. Phys.* **89** 035002

[11] Teufel J D, Donner T, Li D, Harlow J W, Allman M S, Cicak K, Sirois A J, Whittaker J D, Lehnert K W, and Simmonds R W 2011 *Nature* **475** 359

[12] Whittle C, Hall E D, Dwyer S *et al.* 2021 *Science* **372** 1333

[13] Wineland D J and Itano W M 1979 *Phys. Rev. A* **20** 1521

[14] Stenholm S 1986 *Rev. Mod. Phys.* **58** 699

[15] Dalibard J and Cohen-Tannoudji C 1989 *J. Opt. Soc. Am. B* **6** 2023

[16] Mao Z C, Xu Y Z, Mei Q X, Zhao W D, Jiang Y, Wang Y, Chang X Y, He L, Yao L, Zhou Z C, Wu Y K, and Duan L M 2021 *Phys. Rev. Lett.* **127** 143201

[17] Joshi M K, Fabre A, Maier C, Brydges T, Kiesenhofer D, Hainzer H, Blatt R, and Roos C F 2020 *New J. Phys.* **22** 103013

[18] Ejtemaee S and Haljan P C 2017 *Phys. Rev. Lett.* **119** 043001

[19] Morigi G, Eschner J, and Keitel C H 2000 *Phys. Rev. Lett.* **85** 4458

[20] Roos C F, Leibfried D, Mundt A, Schmidt-Kaler F, Eschner J, and Blatt R 2000 *Phys. Rev. Lett.* **85** 5547

[21] Lechner R, Maier C, Hempel C, Jurcevic P, Lanyon B P, Monz T, Brownnutt M, Blatt R, and Roos C F 2016 *Phys. Rev. A* **93** 053401

[22] Diedrich F, Bergquist J C, Itano W M, and Wineland D J 1989 *Phys. Rev. Lett.* **62** 403

[23] Roos C, Zeiger T, Rohde H, Nägerl H C, Eschner J, Leibfried D, Schmidt-Kaler F, and Blatt R 1999 *Phys. Rev. Lett.* **83** 4713

[24] Monroe C, Meekhof D M, King B E, Jefferts S R, Itano W M, Wineland D J, and Gould P 1995 *Phys. Rev. Lett.* **75** 4011

[25] Wineland D, Monroe C, Itano W, Leibfried D, King B, and Meekhof D 1998 *J. Res. Natl. Inst. Stand. Technol.* **103** 259

[26] Chen J S, Wright K, Pisenti N C, Murphy D, Beck K M, Landsman K, Amini J M, and Nam Y 2020 *Phys. Rev. A* **102** 043110

[27] Huang Z, Mundada P S, Gyenis A, Schuster D I, Houck A A, and Koch J 2021 *Phys. Rev. Appl.* **15** 034065

[28] Gandon A, Le Calonnec C, Shillito R, Petrescu A, and Blais A 2022 *Phys. Rev. Appl.* **17** 064006

[29] Deng C, Orgiazzi J L, Shen F, Ashhab S, and Lupascu A 2015 *Phys. Rev. Lett.* **115** 133601

[30] Deng C, Shen F, Ashhab S, and Lupascu A 2016 *Phys. Rev. A* **94** 032323

[31] Wu J L, Wang Y, Han J X, Su S L, Xia Y, Jiang Y, and Song J 2021 *Phys. Rev. A* **103** 012601

[32] Eckardt A 2017 *Rev. Mod. Phys.* **89** 011004

[33] Roy R and Harper F 2017 *Phys. Rev. B* **96** 155118

[34] Peng Y and Refael G 2019 *Phys. Rev. Lett.* **123** 016806

[35] Wintersperger K, Braun C, Ünal F N, Eckardt A, Liberto M D, Goldman N, Bloch I, and Aidelsburger M 2020 *Nat. Phys.* **16** 1058

[36] Peng P, Yin C, Huang X, Ramanathan C, and Cappellaro P 2021 *Nat. Phys.* **17** 444

[37] Yin C, Peng P, Huang X, Ramanathan C, and Cappellaro P 2021 *Phys. Rev. B* **103** 054305

[38] Rechtsman M C, Zeuner J M, Plotnik Y, Lumer Y, Podolsky D, Dreisow F, Nolte S, Segev M, and Szameit A 2013 *Nature* **496** 196

[39] Jotzu G, Messer M, Desbuquois R, Lebrat M, Uehlinger T, Greif D, and Esslinger T 2014 *Nature* **515** 237

[40] Jiménez-García K, LeBlanc L J, Williams R A, Beeler M C, Qu C, Gong M, Zhang C, and Spielman I B 2015 *Phys. Rev. Lett.* **114** 125301

[41] Huang A, Ke S, Guan J H, Li J, and Lou W K 2024 *Chin. Phys. Lett.* **41** 097302

[42] Liu Z R, Chen R, and Zhou B 2024 *Chin. Phys. Lett.* **41** 047102

[43] Bloch F and Siegert A 1940 *Phys. Rev.* **57** 522

[44] Shirley J H 1965 *Phys. Rev.* **138** B979

[45] Wilkason T, Nantel M, Rudolph J, Jiang Y, Garber B E, Swan H, Carman S P, Abe M, and Hogan J M 2022 *Phys. Rev. Lett.* **129** 183202

[46] Wang G, Li C, and Cappellaro P 2021 *Phys. Rev. Lett.* **127** 140604

[47] Hou S Y, Feng G, Wu Z, Zou H, Shi W, Zeng J, Cao C, Yu S, Sheng Z, Rao X, Ren B, Lu D, Zou J, Miao G, Xiang J, and Zeng B 2021 *EPJ Quantum Technol.* **8** 20

[48] Feng G R, Hou S Y, Zou H Y, Shi W, Yu S, Sheng Z K, Rao X, Ma K H, Chen C X, Ren B, Miao G X, Xiang J G, and Zeng B 2022 *IEEE Nanotechnol. Mag.* **16** 20

[49] Zalka C 1998 *Fortschr. Phys.* **46** 877

[50] Cory D G, Fahmy A F, and Havel T F 1997 *Proc. Natl. Acad. Sci. USA* **94** 1634

[51] Zhang J, Zhang M C, Xie Y, Wu C W, Ou B Q, Chen T, Bao W S, Haljan P, Wu W, Zhang S, and Chen P X 2022 *Phys. Rev. Appl.* **18** 014022